25th ABCM International Congress of Mechanical Engineering
October 20-25, 2019, Uberlândia, MG, Brazil

COB-2019-0516
HEMODYNAMIC AND MORPHOLOGICAL CASE STUDY OF AN INTRACRANIAL ANEURYSM INCEPTION AND EVOLUTION

Iago Lessa de Oliveira
José Luiz Gasche
São Paulo State University (UNESP), School of Natural Sciences and Engineering, Ilha Solteira, São Paulo, Brazil
iago.oliveira@unesp.br
jose.gasche@unesp.br

Julio Militzer
Dalhousie University, Department of Mechanical Engineering, Halifax, Nova Scotia, Canada
julio.militzer@dal.ca

Carlos Eduardo Baccin
Interventional Neuroradiology, Hospital Israelita Albert Einstein, São Paulo, Brazil
cebaccin@gmail.com

Abstract. *Aneurysms are dilated and thin regions of arterial walls of the human vascular system. One of the most common type of aneurysm occurs on brain arteries in the circle of Willis. Their cause have been investigated for a long time, and researchers agree that hemodynamic effects play a key role in the initiation, growth, and rupture of brain aneurysms. With the development of scanning techniques of the cerebral vascular system, it has been possible to obtain the geometry of aneurysms, allowing Computational Fluid Dynamics (CFD) to be used for the solution of the blood flow. Since then, several researchers have been investigating the influence of biological and hemodynamic variables on aneurysms rupture, considering arteries and aneurysms as rigid walls. However, fewer studies analyze the initiation and growth of intracranial aneurysms and the importance of hemodynamics in this process, probably due to the lack of availability of consecutive exams of a single aneurysm case. In this work, by using two available exams at different instants of time of a single aneurysm case and also by virtually reconstructing the healthy vasculature, we used CFD results to assess whether hemodynamic parameters can be correlated with aneurysm initiation and growth.*

Keywords: ***Intracranial aneurysms. Aneurysm evolution. Hemodynamic. Numerical simulation***

1. INTRODUCTION

An intracranial aneurysm is a pathological dilatation in the vascular system occurring in the arteries that reach the brain; they are normally found in bifurcations of the vessels tree (terminal aneurysms) or laterally to the arteries (sidewall aneurysms, Fig. 1). They are normally asymptomatic and represent a high risk to the patient if they rupture: one of the most dangerous and common outcomes is the subarachnoid hemorrhage (SAH), a devastating event that in 85 % of cases is caused by aneurysm rupture (van Gijn *et al.*, 2001) and can be fatal – Hop *et al.* (1997) show that this occurs in 32 % to 67 % of cases and about one-third of morbidity among the patients who survived. Interestingly, not every aneurysm do rupture, in fact, most of them stabilize.

Although in very early studies aneurysms were thought to be possibly congenital (Stehbens, 1989), it is widely accepted today that they are acquired lesions related to the interaction between the hemodynamic environment in the aneurysm lumen and its wall, being the wall shear stress (WSS) one of the most important factors related to their progression (Hashimoto *et al.*, 2006; Tremmel *et al.*, 2009; Fukazawa *et al.*, 2015; Cebral *et al.*, 2017). While aneurysm onset is normally accepted to be related to high WSS levels, their growth and final rupture or stabilization is explained by two pathways correlating hemodynamics and aneurysm progression. Meng *et al.* (2014), for example, go further and relate these two pathways with different morphological features that may arise in the aneurysm wall.

In this context, CFD has been widely used to simulate the flow in virtual and patient-specific aneurysms geometries and vessel networks. The simulations have been used to improve the understanding of the flow dynamics and to correlate morphological and hemodynamic discriminants with aneurysm rupture (Ma *et al.*, 2004; Dhar *et al.*, 2008; Xiang *et al.*, 2011; Cebral *et al.*, 2011b,a). While several CFD studies were performed on aneurysm geometries of a single instant in time, few studies have considered the time evolution of intracranial aneurysms, but the ones that do only had available

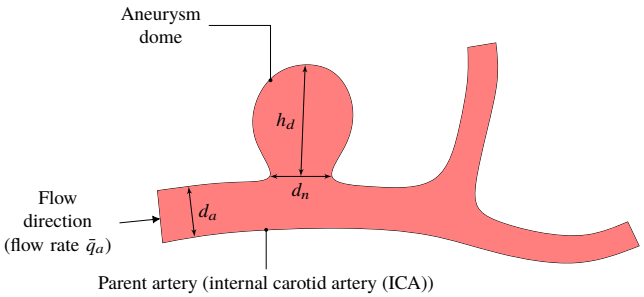

Figure 1. Typical lateral intracranial aneurysm occurring on the ICA, with indications of its main one-dimensional sizes: aneurysm dome height, h_d, and d_n, the neck diameter; the parent artery has diameter d_a.

a single geometry of the aneurysm temporal evolution (Boussel *et al.*, 2008; Sforza *et al.*, 2011), possibly because most available exams used are retrospective. Additionally, when physicians detect an aneurysm, they may of course decide to treat the aneurysm. This study used the images of a growing sidewall intracranial aneurysm at two instants in time and its parent vessel reconstructed geometry to analyze the hemodynamics of the aneurysm lumen and its wall, and the peri-aneurysmal environment, looking for possible correlations between hemodynamics and aneurysm initiation and growth. Therefore, we could study the hemodynamic conditions at initiation and during the growth period of three years.

2. METHODOLOGY

2.1 Images and geometry segmentation

The intracranial aneurysm geometry selected was chosen because of the availability of two successive geometries corresponding to two digital subtraction angiography (DSA) exams collected retrospectively. It corresponds to a saccular sidewall aneurysm born in the ophthalmic segment of the ICA siphon, a common location of this kind of aneurysm.

The geometries of the vessels network and the aneurysm were segmented using the Vascular Modeling Toolkit® (VMTK®) library with the level-sets segmentation approach (Piccinelli *et al.*, 2009). Figures 2b and 2c show the aneurysm geometry on the ICA inner bend at two different stages, labeled T1 and T2, which were extracted from exams taken with an interval of three years between each other – in 2015 and 2018, respectively. A large portion of the ICA and the daughter arteries – the anterior cerebral artery (ACA) and the middle cerebral artery (MCA) – were included to avoid the influence of the inlet and outlets positions on the intra-aneurysmal and peri-aneurysmal flow (Chnafa *et al.*, 2018). The hypothetical healthy artery was reconstructed by virtually removing the aneurysm at stage T1 by applying a local Laplacian filter on the aneurysm portion, i.e. the aneurysm surface was consecutively smoothed until only the parent artery remained; the final reconstructed healthy vasculature is shown in Fig. 2a. This technique was chosen to avoid the influence of the smoothing in the surrounding vasculature. Table 1 provides the geometric parameters of the aneurysm at each stage.

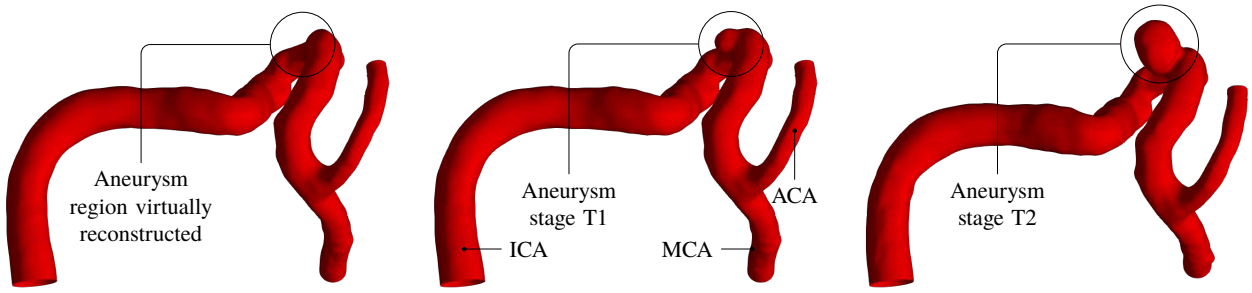

(a) (b) (c)

Figure 2. Vessels network geometries used for the simulations: (a) vessels network virtually reconstructed labeled stage T0; (b) vessels network and aneurysm geometry at the T1 stage, and (c) vessels network and aneurysm geometry at the T2 stage.

Table 1. Geometric parameters of the aneurysm studied here: neck diameter d_n, dome height h_d and diameter d_d, aspect ratio A_r, and aneurysm volume and surface area.

	d_n (mm)	h_d (mm)	d_d (mm)	A_r (-)	V_a (mm^3)	A_a (mm^2)
Stage T1	2.82	1.79	2.33	0.63	5.4	18.2
Stage T2	2.87	4.42	4.11	1.54	37.5	57.8

The computational meshes were created using the utility `snappyHexMesh` of the CFD package `foam-extend-4.0`, which generates hexahedral-dominant meshes by snapping a block-structured mesh to the surface geometry and automatically creating a refined prismatic boundary-layer adjacent to the vessels and aneurysm lumen surface. The computational meshes had approximately 4×10^6 control volumes and the final chosen mesh for each case was the result of a mesh-independence test.

2.2 Physical and Mathematical Model of the Blood Flow

We consider the blood as an incompressible fluid in an isothermal laminar flow regime. The equations governing its motion are the continuity equation, written in the integral form for a control volume V, with surface S, as:

$$\oint_S \rho \boldsymbol{v} \cdot \boldsymbol{n} \mathrm{d}S = 0, \tag{1}$$

where $\rho = 1{,}056\,\mathrm{kg/m^3}$ is the blood specific mass (Isaksen *et al.*, 2008), $\boldsymbol{n}$ is the unit normal vector to S pointing outwards and $\boldsymbol{v}$ is the flow velocity field; and the momentum equation, written in the integral conservative form as:

$$\frac{\partial}{\partial t}\int_{V(t)} \rho \boldsymbol{v}\,(\boldsymbol{x}, t)\mathrm{d}V + \oint_{S(t)} \rho \boldsymbol{v}\boldsymbol{v} \cdot \boldsymbol{n} \mathrm{d}S = -\oint_{S(t)} p\boldsymbol{n}\mathrm{d}S + \oint_{S(t)} \boldsymbol{\tau} \cdot \boldsymbol{n}\mathrm{d}S, \tag{2}$$

where p is the pressure and $\boldsymbol{\tau}$ is the viscous part of the Cauchy stress tensor, which for a Newtonian fluid is given by:

$$\boldsymbol{\tau} = \mu^f \left(\nabla \boldsymbol{v} + \nabla^{\mathrm{T}} \boldsymbol{v}\right), \tag{3}$$

where μ^f is the blood dynamic viscosity, which we considered to be 3.5×10^{-3} Pa s (Shibeshi and Collins, 2005; Isaksen *et al.*, 2008). Equation (3) can be directly substituted into Eq. (2) to yield the Navier-Stokes equations.

We used a trivial initial condition for the velocity and pressure fields. At the inlet, a specified time-varying blood flow rate, corresponding to the flow pulse from the beginning of systole until the end of the diastole (Fig. 3) was imposed, obtained by using the normalized waveform profile based on the temporal average blood flow rate measured in the internal carotid by Ford *et al.* (2005), and the average blood flow rate, $\bar{q}_a = 4.3\,\mathrm{ml/s}$, in the ICA, measured by Zarrinkoob *et al.* (2015). It is important to note that this profile does not correspond to the patient-specific blood flow rate waveform at the ICA, which was not available. Furthermore, we used a parabolic velocity profile, perpendicular to the cross section (plane xy), corresponding to a fully developed laminar flow in a pipe given by:

$$\boldsymbol{v}_{inlet}\,(x, y) = 2\frac{\bar{q}_a}{A_{inlet}}\left[1 - \frac{4}{d_a^2}\left(x^2 + y^2\right)\right], \tag{4}$$

where A_{inlet} is the cross sectional area of the inlet artery and d_a is its diameter – we added a flow extension to the artery inlet section to obtain a circular section to impose this inlet flow condition. Additionally, the pressure gradient was set to zero at the inlet. At the outlet sections, to obtain the correct pressure in the results, we imposed a constant pressure, corresponding to the averaged human body pressure level for a cardiac cycle, i.e. $\approx 100\,\mathrm{mmHg}$ (13,333 Pa), and a flux-corrected zero gradient velocity. The vessels walls were considered rigid, yielding a Dirichlet boundary condition for the velocity field, associated with zero mass flux, zero pressure gradient, and the no-slip condition.

To solve Eqs. (1) and (2) with the fluid model, Eq. (3), under the boundary conditions presented above, we chose the Finite Volume Method (FVM) implemented in the open-source package `foam-extend`, version 4.0, which provides a second-order accurate spatial and temporal discretizations of the governing equations and, to assure this accuracy level, we also selected second-order interpolation profiles available in the library. The time-step used in the simulations was 1×10^{-5} s, which was validated through a time-step independence test. We solved three cardiac cycles to avoid initial transient errors, but only the third one was analyzed in the results. Finally, the pressure-velocity coupling algorithm used was the Pressure Implicit with Splitting Operators (PISO) (Issa, 1986).

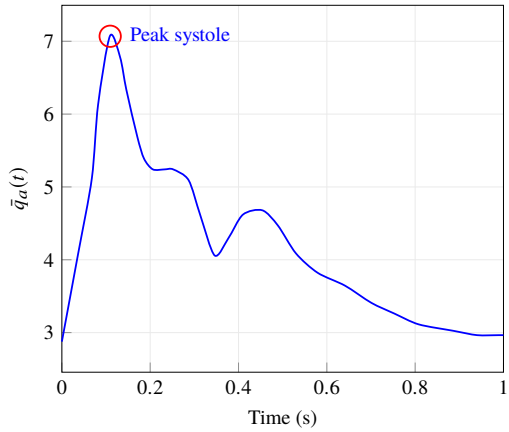

Figure 3. Time-varying flow rate waveform in the internal carotid artery (prepared by the authors with data from Ford *et al.* (2005) and Zarrinkoob *et al.* (2015).

2.3 Data Reduction

We analyzed the WSS field at the peak systole – indicated by a red circle in Fig. 3 – and its time-averaged metric together with the oscillatory shear index (OSI) field, both defined, respectively, as:

$$\overline{t_w}\,(\boldsymbol{x}) = \frac{1}{T}\int_0^T \|\boldsymbol{t}_w\,(\boldsymbol{x},t)\|_2 \mathrm{d}t \tag{5}$$

and

$$OSI\,(\boldsymbol{x}) = \frac{1}{2}\left(1 - \frac{\left\|\int_0^T \boldsymbol{t}_w\,(\boldsymbol{x},t)\,\mathrm{d}t\right\|}{\int_0^T \|\boldsymbol{t}_w\,(\boldsymbol{x},t)\|_2 \mathrm{d}t}\right), \tag{6}$$

where T is the cardiac cycle period. In the sequence, WSS and OSI metrics were calculated over the aneurysm surface: the time and surface averaged WSS and OSI:

$$(t_w)_{avg} = \frac{1}{A_a}\int_{S_a} \overline{t_w}\,(\boldsymbol{x})\,\mathrm{d}S_a\,, \tag{7}$$

$$OSI_{avg} = \frac{1}{A_a}\int_{S_a} OSI\,(\boldsymbol{x})\,\mathrm{d}S_a\,, \tag{8}$$

and their maximum averaged values on the aneurysm surface:

$$(t_w)_{max} = \max_{\boldsymbol{x}\in S_a} \overline{t_w}\,(\boldsymbol{x})\,, \tag{9}$$

$$OSI_{max} = \max_{\boldsymbol{x}\in S_a} OSI\,(\boldsymbol{x})\,. \tag{10}$$

Finally, the surface-averaged WSS on the aneurysm surface over time was also computed and analyzed for each case:

$$\langle t_w\rangle\,(t) = \frac{1}{A_a}\int_S \|\boldsymbol{t}_w\|\,\mathrm{d}S_a\,, \tag{11}$$

which provides the total tangential viscous traction on aneurysm lumen surface. We compared the WSS values with the reference $WSS = 1.5$ Pa because smaller values could damage the aneurysm wall tissue (Malek *et al.*, 1999; Shojima *et al.*, 2004).

3. RESULTS

Figure 4 shows the WSS field at the peak systole of the cardiac cycle – $t \approx 0.11$ s – and the time-averaged WSS over one cardiac cycle: fields over the complete surface and a detail showing the aneurysm region only are presented. We note that the overall WSS is much higher than the reference value of 1.5 Pa, for both stages of the aneurysm evolution at the peak systole instant. However, for stage T2, the regions with low levels of WSS are larger. By inspecting the region of the artery where the aneurysm initiates (Figs. 4a and 4d), we note that the WSS levels are initially very high – higher than 20 Pa. However, it can be seen that the time averaged WSS levels for stage T2 are much smaller – from 8 Pa to 12 Pa – compared with stages T0 and T1 – WSS levels above 20 Pa. The surface-averaged WSS also decreases over time (Fig. 5) evidencing that the low WSS regions are larger on the aneurysm at later stages, therefore influencing the whole distribution.

The larger areas of low WSS are explained by the intra-aneurysmal flow type: as we can see in Fig. 6, at stage T1, due to the aneurysm type, a recirculation zone begins to form inside the aneurysm sac. After the aneurysm evolution to stage T2, the slow recirculating zone occupies the whole aneurysm sac with smaller velocity magnitudes. This is a typical flow structure that occurs in this type of aneurysm and yields smaller velocity levels in the aneurysm lumen and, consequently, decreasing the WSS levels on its inner surface.

The quantitative change of the WSS and OSI over time can be measured by using the metrics presented for both of them in Section 2.3. Figure 7 shows the surface and time averaged values of WSS and OSI over the aneurysm surface for each development stage – for T0, we used the artery portion where the aneurysm effectively developed for the calculations, equivalent to its future ostium surface. It is evident that the overall WSS is decreasing on the aneurysm surface because of the increase in the areas of low WSS, however its maximum value is growing over time; this is probably occurring because the remaining patches with high WSS values are even higher then before due to the complex flow patterns inside the aneurysm sac.

We also analyzed the OSI field over the aneurysm surface at the stages T1 and T2 showing that small patches of the aneurysm surface are under the effect of higher OSI – i.e. values close to its maximum, 0.5 – in regions where the WSS

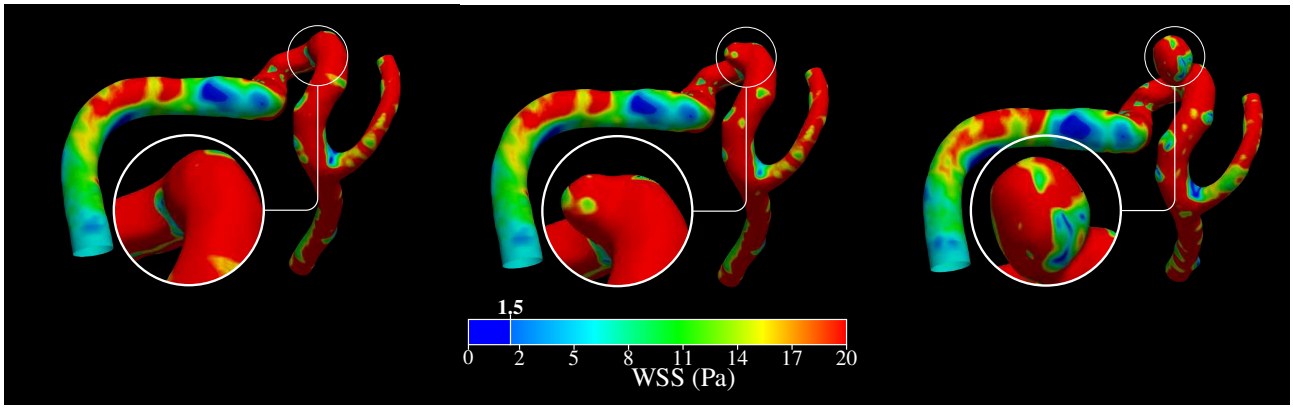

(a) (b) (c)

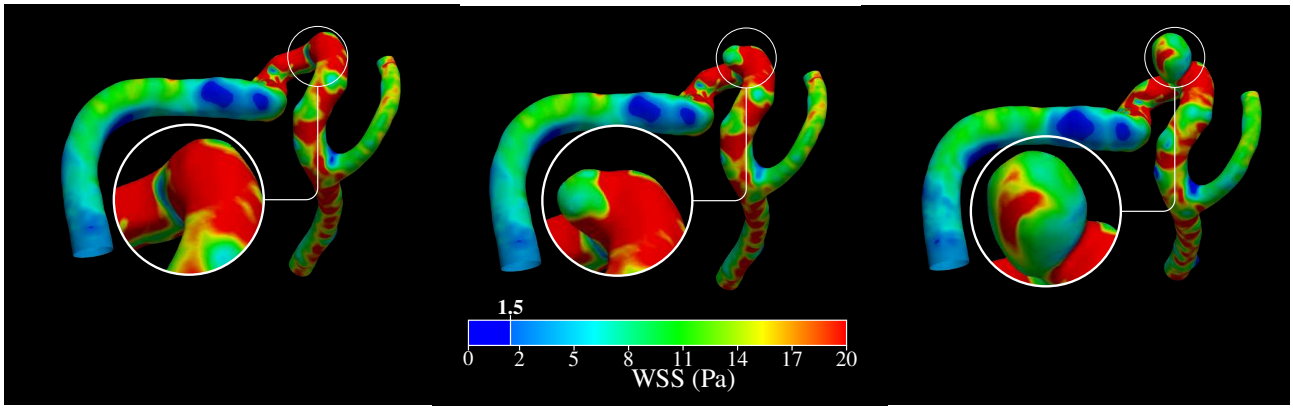

(d) (e) (f)

Figure 4. WSS field over the complete surface and detail of the aneurysm surface at peak systole for stages (a) T0, (b) T1, and (c) T2; and time-averaged WSS field over the complete surface and detail of the aneurysm surface for stages (d) stage T0, (e) stage T1, and (f) stage T2.

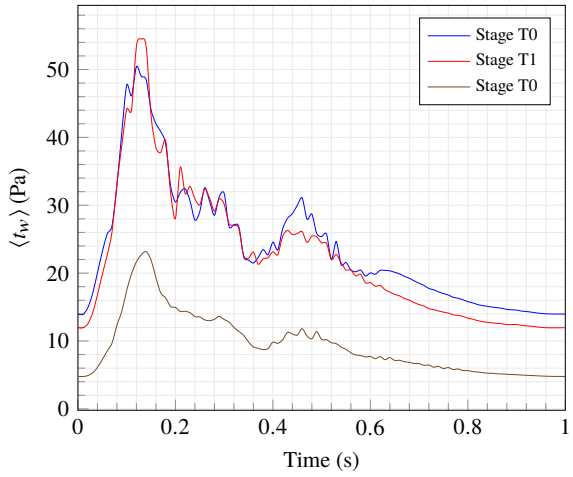

Figure 5. Surface-averaged WSS over one cardiac cycle for each stage, evidencing the decrease in the WSS for the whole cardiac cycle.

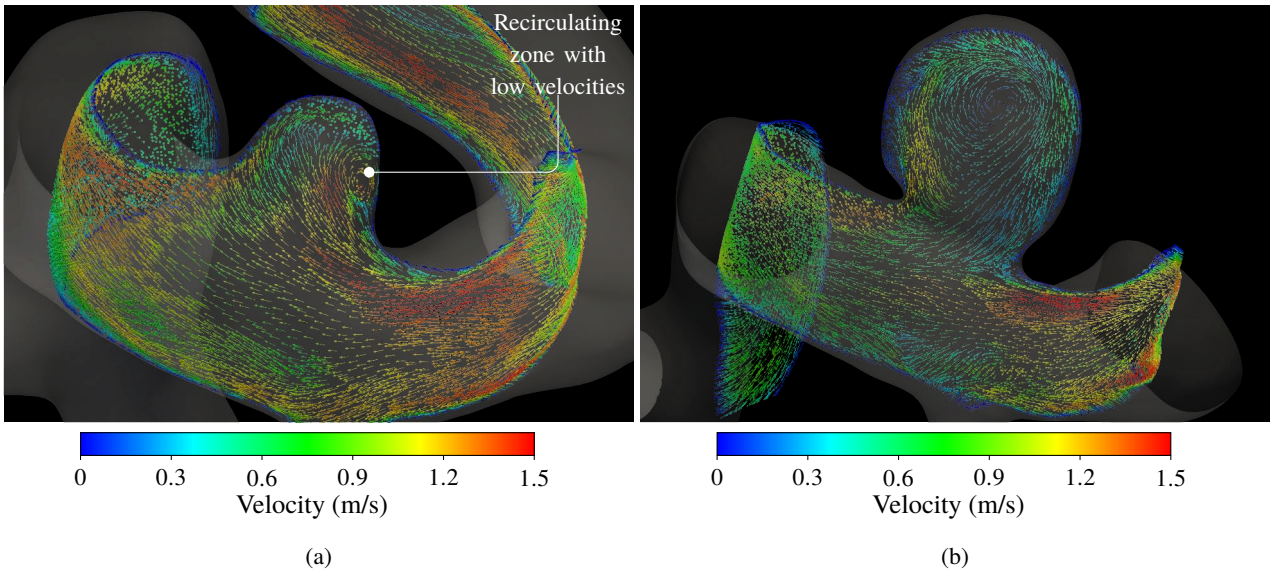

Figure 6. Flow velocity vector field in (a) the aneurysm at stage T1 and (b) at stage T2.

vector changes its direction over time during a cardiac cycle, evidencing the disturbed flow adjacent to the aneurysm lumen. As these areas are still very small, we do not show the fields here, however they contribute to the surface-averaged OSI increase on the aneurysm surface, as can be seen in Fig. 7c.

Finally, to further explore a possible correlation between WSS and aneurysm growth, we computed the point-wise distance between the aneurysm surfaces in stages T1 and T2 and compared it with the time-averaged WSS field. These fields are shown in Fig. 8: the "growth distance" corresponds to the distance that the aneurysm has grown in the three years between each exam. We note that the regions of maximum aneurysm growth, which in this case occurred at the aneurysm dome, is dominated by lower WSS values – between 5 Pa and 11 Pa.

4. DISCUSSION

Despite a cause for intracranial aneurysm rupture is one of the most searched subjects in current related researches, their initiation and growth have also been investigated in past years. Most studies agree that intracranial aneurysms inception occurs due to high flow effects acting on the vessels surface together with positive WSS spatial gradients (Meng *et al.*, 2014). Meng *et al.* (2007), for example, observed destructive remodeling of dog artery walls that resembled aneurysm type remodeling after a surgically created bifurcation in the dog's arteries. While their study focused on bifurcation aneurysms, it is also generally accepted that sidewall aneurysms initiates in regions of high WSS and positive WSS spatial gradient (Geers *et al.*, 2017). Lauric *et al.* (2014), for example, explored the influence of the ICA local curvature on the onset of sidewall aneurysms (all their cases were of lateral aneurysms in the inner bend of the ICA), similar to the case studied here,

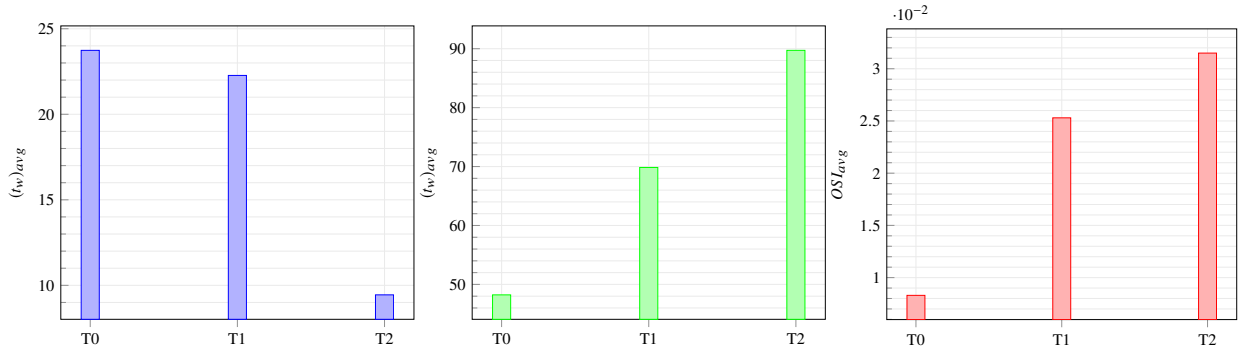

(a) (b) (c)

Figure 7. WSS and OSI metrics over the aneurysm surface: (a) time and surface averaged WSS, (b) maximum time-averaged WSS, and (c) surface-averaged OSI.

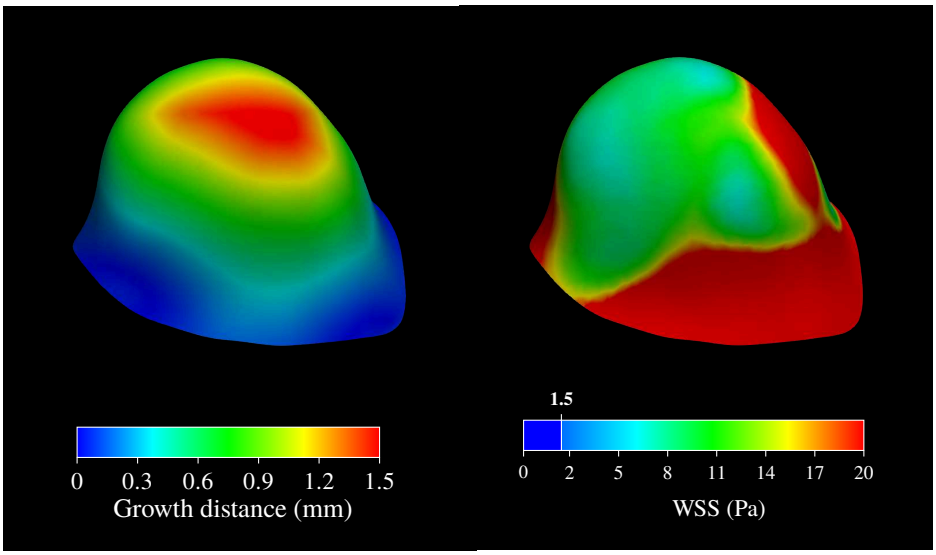

(a) (b)

Figure 8. Spatial correlation between growth distance and time-averaged WSS over the aneurysm at T1: (a) the growth distance array measured between the aneurysm surfaces in stages T1 and T2 by surface registration and (b) time-averaged WSS over the aneurysm at stage T1.

by virtually reconstructing the hypothetical healthy parent artery. Their conclusions suggests that peak local curvatures correlate with regions of high WSS and flanked by high and positive WSS spatial gradient in the arteries that developed an aneurysm – in contrast with control arteries, i.e. healthy arteries with similar morphological features. The results for the case studied here agrees with their findings: very high WSS values – more than 20 Pa – were found in the aneurysmal region at stage T0. Furthermore, we note from the time-averaged WSS on the ICA bend (Fig. 4d), that the region where the aneurysm will form is predominantly marked with high WSS while the surrounding areas have large portions of smaller WSS, meaning that throughout the cardiac cycle these regions are influenced by low WSS.

Regarding aneurysm growth, there is no consensus in the literature about a single mechanism responsible for it, on the contrary, the literature suggests two pathways that drive aneurysms evolution: low-flow and high-flow effects (Meng *et al.*, 2014). In general, the former is accepted to be caused by lower WSS values with high OSI in the aneurysm surface and the latter is caused by high WSS and high positive WSS spatial gradients. Of course, due to the complex flow that may emerge inside an aneurysm lumen depending on its morphology, both effects can occur on an aneurysm surface. Our results suggest that in this aneurysm evolution occurred mainly due to lower WSS values on the aneurysm surface because, even if at the peak systole the values are very high at stage T1, the time-averaged WSS suggests that lower WSS affects the aneurysm surface throughout the cardiac cycle (Fig. 8). Furthermore, it is also worth noting that this aneurysm evolved in a spherical shape, which suggests that the growth was due to only a single effect, instead of different mechanisms that would probably lead to blebs or lobular regions on its surface (Tateshima *et al.*, 2003). However, our results do not suggest a significant influence of the OSI in the aneurysm growth since this variable shows only local peaks in small portions of

the surface.

Although several studies suggest that aneurysm inception is caused by high flow effects, some studies propose new hemodynamic parameters that indicate where an aneurysm will grow (Mantha *et al.*, 2006; Shimogonya *et al.*, 2009). Mantha *et al.* (2006), for example, studied the initiation of three paraclinoid sidewall aneurysms by virtually reconstructing the healthy artery, and proposed a new parameter to identify aneurysm inception: the (potential) aneurysm formation indicator (AFI), which measures the degree of misalignment of the instantaneous WSS vector with its time-averaged direction; they based this definition on the biological observation that healthy endothelial cells are oriented according to the averaged WSS vector direction and, consequently, randomly oriented vectors during the cardiac cycle could "trigger pathological changes in the endothelial cells, leading to aneurysm formation." Their results suggest that the aneurysm formation occurs in regions of low AFI – i.e. $AFI \approx -1.0$.

We computed the AFI parameter for the vascular geometry used here; however, we did not find a correlation between the regions of low AFI with the location of aneurysm initiation, as also found, for example, by Chen *et al.* (2013) and Geers *et al.* (2017). Moreover, as shown by Geers *et al.* (2017), OSI and AFI fields are strongly correlated implying, hence, that these variables capture the same flow features generated on the aneurysm surface. Thus, since OSI does not seem to play a role in the aneurysm formation for the case studied here, it is understandable that the AFI yields a similar conclusion.

4.1 Limitations of this study

A very common limitation of several CFD studies in intracranial aneurysm flow are the boundary conditions. Since a patient-specific cardiac profile was not available, we used a population-averaged inlet boundary condition, and some studies suggest that it may be very important to consider the patient blood flow profile since it highly influences the WSS magnitude distribution (Marzo *et al.*, 2011). However, to diminish these effects, we remember that the chosen profile was measured exactly in the ICA and we extracted a large portion of the parent artery to allow the flow development according to the real structure of the patient's vasculature and used a parabolic spatial velocity profile. We also used constant pressure outlet boundary conditions, however, by further extending the outlets position downstream the vasculature from the aneurysm location, we approximate an outflow resistance condition (Chnafa *et al.*, 2018).

The healthy vasculature geometry was virtually reconstructed bu using a local smoothing technique which is performed manually and thus it can be operator dependent. Unfortunately, an image with the healthy artery of this specific patient was not available, and we chose this option to preserve the surrounding vasculature. However, we can expect that the overall geometry would remain the same between stages T0 and T1 because they are almost identical when we compare the vascular geometry of stages T1 and T2 – except for possible differences arising from the segmentation process.

5. CONCLUSIONS

This study analyzed the flow dynamics in an intracranial aneurysm case, and investigated the influence of hemodynamic parameters in the initiation and growth of the aneurysm by using two available DSA exams from a single patient at two instants in time. It is worth to note that this kind of study seems to be a perfect example of how CFD can be a complementary tool to clinically study aneurysms cases. With this kind of study, a complete description of the flow is obtained and important variables such as WSS and OSI, that are known to play crucial roles in this pathology, can be computed. Of course, as suggested in literature discussions (Cebral and Meng, 2012), CFD should be included in the medical practice with warnings of its limitations, simplifications and complexities.

6. ACKNOWLEDGEMENTS

This research is supported by grant 2017/18514-1 São Paulo Research Foundation (FAPESP); it was also partly supported by resources supplied by the Center for Scientific Computing (NCC/GridUNESP) of the São Paulo State University (UNESP) and Acenet (Dalhousie University).

7. REFERENCES

Boussel, L., Rayz, V., Mcculloch, C., Martin, A., Acevedo-Bolton, G., Lawton, M., Higashida, R., Smith, W.S., Young, W.L. and Saloner, D., 2008. "Aneurysm Growth Occurs at Region of Low Wall Shear Stress: Patient-Specific Correlation of Hemodynamics and Growth in a Longitudinal Study". *Stroke*, Vol. 39, pp. 2997–3002. doi:10.1161/STROKEAHA.108.521617. URL `http://stroke.ahajournals.org`.

Cebral, J., Ollikainen, E., Chung, B.J., Mut, F., Sippola, V., Jahromi, B.R., Tulamo, R., Hernesniemi, J., Niemelä, M., Robertson, A. and Frösen, J., 2017. "Flow conditions in the intracranial aneurysm lumen are associated with inflammation and degenerative changes of the aneurysm wall". *American Journal of Neuroradiology*, Vol. 38, No. 1. doi:10.3174/ajnr.A4951.

Cebral, J.R., Mut, F., Weir, J. and Putman, C., 2011a. "Quantitative characterization of the hemodynamic environment

in ruptured and unruptured brain aneurysms". *American Journal of Neuroradiology*, Vol. 32, pp. 145–151. doi: 10.3174/ajnr.A2419.

Cebral, J.R., Mut, F., Weir, J. and Putman, C.M., 2011b. "Association of hemodynamic characteristics and cerebral aneurysm rupture". *American Journal of Neuroradiology*, Vol. 32, pp. 264–270. doi:10.3174/ajnr.A2274.

Cebral, J.R. and Meng, H., 2012. "Counterpoint: Realizing the Clinical Utility of Computational Fluid Dynamics—Closing the Gap". doi:10.3174/ajnr.a2993.

Chen, H., Selimovic, A., Thompson, H., Chiarini, A., Penrose, J., Ventikos, Y. and Watton, P.N., 2013. "Investigating the Influence of Haemodynamic Stimuli on Intracranial Aneurysm Inception". *Annals of Biomedical Engineering*, Vol. 41, No. July, pp. 1492–1504. doi:10.1007/s10439-013-0794-6.

Chnafa, X.C., Brina, X.O., Pereira, V.M. and Steinman, X.D.A., 2018. "Better Than Nothing: A Rational Approach for Minimizing the Impact of Outflow Strategy on Cerebrovascular Simulations". *American Journal of Neuroradiology*, Vol. 39, pp. 337–343. doi:10.3174/ajnr.A5484. URL `http://dx.doi.org/10.3174/ajnr.A5484`.

Dhar, S., Tremmel, M., Mocco, J., Kim, M., Yamamoto, J., Siddiqui, A.H., Hopkins, L.N. and Meng, H., 2008. "Morphology parameters for intracranial aneurysm rupture risk assessment". *Neurosurgery*, Vol. 63, No. 2, pp. 185–196. doi:10.1227/01.NEU.0000316847.64140.81.

Ford, M.D., Alperin, N., Lee, S.H., Holdsworth, D.W. and Steinman, D.A., 2005. "Characterization of volumetric flow rate waveforms in the normal internal carotid and vertebral arteries". *Physiological Measurement*, Vol. 26, No. 4, pp. 477–488. doi:10.1088/0967-3334/26/4/013.

Fukazawa, K., Ishida, F., Umeda, Y., Miura, Y., Shimosaka, S., Matsushima, S., Taki, W., Suzuki, H., Bligh, M. and Others, 2015. "Using computational fluid dynamics analysis to characterize local hemodynamic features of middle cerebral artery aneurysm rupture points". *World Neurosurgery*, Vol. 83, No. 1, pp. 80–86. doi:10.1016/j.wneu.2013.02.012.

Geers, A.J., Morales, H.G., Larrabide, I., Butakoff, C., Bijlenga, P. and Frangi, A.F., 2017. "Wall shear stress at the initiation site of cerebral aneurysms". *Biomechanics and Modeling in Mechanobiology*, Vol. 16, pp. 97–115. doi:10.1007/s10237-016-0804-3.

Hashimoto, T., Meng, H. and Young, W.L., 2006. "Intracranial aneurysms: links among inflammation, hemodynamics and vascular remodeling". *Neurological Research*, Vol. 28, pp. 372–380. doi:10.1179/016164106X14973.

Hop, J.W., Rinkel, G.J.E., Algra, A. and van Gijn, J., 1997. "Case-Fatality Rates and Functional Outcome After Subarachnoid Hemorrhage". *Stroke*, Vol. 28, No. 3, pp. 660 – 664. URL `http://stroke.ahajournals.org/content/28/3/660.abstract`.

Isaksen, J.G., Bazilevs, Y., Kvamsdal, T., Zhang, Y., Kaspersen, J.H., Waterloo, K., Romner, B. and Ingebrigtsen, T., 2008. "Determination of wall tension in cerebral artery aneurysms by numerical simulation". *Stroke*, Vol. 39, No. 12, pp. 3172–3178. ISSN 00392499. doi:10.1161/STROKEAHA.107.503698.

Issa, R.I., 1986. "Solution of the implicitly discretised fluid flow equations by operator-splitting". *Journal of Computational Physics*, Vol. 62, No. 1, pp. 40–65. ISSN 10902716. doi:10.1016/0021-9991(86)90099-9.

Lauric, A., Hippelheuser, J., Safain, M.G. and Malek, A.M., 2014. "Curvature effect on hemodynamic conditions at the inner bend of the carotid siphon and its relation to aneurysm formation". *Journal of Biomechanics*, Vol. 47, No. 12, pp. 3018–3027. doi:10.1016/j.jbiomech.2014.06.042. URL `http://dx.doi.org/10.1016/j.jbiomech.2014.06.042`.

Ma, B., Harbaugh, R.E. and Raghavan, M.L., 2004. "Three-dimensional geometrical characterization of cerebral aneurysms." *Annals of biomedical engineering*, Vol. 32, No. 2, pp. 264–273. ISSN 0090-6964.

Malek, A.M., Alper, S.L. and Izumo, S., 1999. "Hemodynamic Shear Stress and Its Role in Atherosclerosis". *Journal of the American Medical Association*, Vol. 282, No. December, pp. 2035–2042.

Mantha, A., Karmonik, C., Benndorf, G., Strother, C. and Metcalfe, R., 2006. "Hemodynamics in a Cerebral Artery before and after the Formation of an Aneurysm". *American Journal of Neuroradiology*, Vol. 27, No. May, pp. 1113–1118. URL `www.ajnr.org`.

Marzo, A., Singh, P., Larrabide, I., Radaelli, A., Coley, S., Gwilliam, M., Wilkinson, I.D., Lawford, P., Reymond, P., Patel, U., Frangi, A. and Hose, D.R., 2011. "Computational Hemodynamics in Cerebral Aneurysms: The Effects of Modeled Versus Measured Boundary Conditions". *Annals of Biomedical Engineering*, Vol. 39, No. 2, pp. 884–896. doi:10.1007/s10439-010-0187-z.

Meng, H., Tutino, V.M., Xiang, J. and Siddiqui, A., 2014. "High WSS or Low WSS? Complex interactions of hemodynamics with intracranial aneurysm initiation, growth, and rupture: Toward a unifying hypothesis". *American Journal of Neuroradiology*, Vol. 35, No. 7, pp. 1254–1262. ISSN 1936959X. doi:10.3174/ajnr.A3558.

Meng, H., Wang, Z., Hoi, Y., Gao, L., Metaxa, E., Swartz, D.D., Kolega, J., Swartz, D.D. and Kolega, J., 2007. "Complex Hemodynamics at the Apex of an Arterial Bifurcation Induces Vascular Remodeling Resembling Cerebral Aneurysm Initiation". *Stroke*, Vol. 38, pp. 1924–1931. doi:10.1161/STROKEAHA.106.481234.

Piccinelli, M., Veneziani, A., Steinman, D.A., Remuzzi, A. and Antiga, L., 2009. "A framework for geometric analysis of vascular structures: Application to cerebral aneurysms". *IEEE Transactions on Medical Imaging*, Vol. 28, No. 8, pp. 1141–1155. doi:10.1109/TMI.2009.2021652.

Sforza, D.M., Putman, C., Tateshima, S., Viñuela, F. and Cebral, J., 2011. "Time evolution and hemodynamics of cerebral aneurysms". In *Proceedings of SPIE*. ISBN 9780819485076. ISSN 16057422. doi:10.1117/12.877703.

Shibeshi, S.S. and Collins, W.E., 2005. "The Rheology of Blood Flow in a Branched Arterial System with Three-Dimensional Model: A Numerical Study". *Applied Rheology*, Vol. 15, No. 6, pp. 398–405. doi:10.1017/S1727719100002951.

Shimogonya, Y., Ishikawa, T., Imai, Y., Matsuki, N. and Yamaguchi, T., 2009. "Can temporal fluctuation in spatial wall shear stress gradient initiate a cerebral aneurysm? A proposed novel hemodynamic index, the gradient oscillatory number (GON)". *Journal of Biomechanics*, Vol. 42, pp. 550–554.

Shojima, M., Oshima, M., Takagi, K., Torii, R., Hayakawa, M., Katada, K., Morita, A. and Kirino, T., 2004. "Magnitude and Role of Wall Shear Stress on Cerebral Aneurysm. Computational Fluid Dynamic Study of 20 Middle Cerebral Artery Aneurysms". *Stroke*, Vol. 35, No. 11, pp. 2500–2505. ISSN 0039-2499. doi:10.1161/01.STR.0000144648.89172.of. URL http://stroke.ahajournals.org/cgi/doi/10.1161/01.STR.0000144648.89172.of.

Stehbens, W.E., 1989. "Etiology of intracranial berry aneurysms". *Journal of Neurosurgery*, Vol. 70, pp. 823–831. ISSN 0022-3085. doi:10.3171/jns.1989.70.6.0823.

Tateshima, S., Murayama, Y., Villablanca, J.P., Morino, T., Nomura, K., Tanishita, K. and Viñuela, F., 2003. "In vitro measurement of fluid-induced wall shear stress in unruptured cerebral aneurysms harboring blebs". *Stroke*, Vol. 34, No. 1, pp. 187–192. doi:10.1161/01.STR.0000046456.26587.8B.

Tremmel, M., Dhar, S., Levy, E.I., Mocco, J. and Meng, H., 2009. "Influence of intracranial aneurysm-to-parent vessel size ratio on hemodynamics and implication for rupture: Results from a virtual experimental study". *Neurosurgery*, Vol. 64, pp. 622–633. doi:10.1227/01.NEU.0000341529.11231.69.

van Gijn, J., Rinkel, G.J.E., Gijn, J.V. and Rinkel, G.J.E., 2001. "Subarachnoid haemorrhage: diagnosis, causes and management." *Brain : a journal of neurology*, Vol. 124, No. Pt 2, pp. 249–78. doi:10.1093/brain/124.2.249. URL http://www.ncbi.nlm.nih.gov/pubmed/11157554.

Xiang, J., Natarajan, S.K., Tremmel, M., Ma, D., Mocco, J., Hopkins, L.N., Siddiqui, A.H., Levy, E.I. and Meng, H., 2011. "Hemodynamic-morphologic discriminants for intracranial aneurysm rupture". *Stroke*, Vol. 42, No. 1, pp. 144–152. ISSN 00392499. doi:10.1161/STROKEAHA.110.592923.

Zarrinkoob, L., Ambarki, K., Wåhlin, A., Birgander, R., Eklund, A. and Malm, J., 2015. "Blood flow distribution in cerebral arteries". *Journal of Cerebral Blood Flow and Metabolism*, Vol. 35, pp. 648–654. ISSN 15597016. doi:10.1038/jcbfm.2014.241.

8. RESPONSIBILITY NOTICE

The authors are the solely responsible for the printed material included in this paper.